



OPEN Sapphire/silicon-substrate dependent magnetism of Er-substituted ZnO (ZnO: Er) thin film: x-ray absorption near edge structure (XANES) study

Shivani Das¹, Kuan-Hung Chen², Tapaswini Chhotaray¹, Wei-Xuan Lin², Surajit Ghosh², Dilip Kumar Mishra¹, Sekhar Chandra Ray^{1,3}✉ & W. F. Pong²✉

Hexagonal wurtzite structure Er-substituted ZnO dilute magnetic semiconductors (DMSs) thin films have been deposited on sapphire/silicon substrate [(ZnO: Er)_{sapphire/silicon}] using DC sputtering technique at room temperature in oxygen-plasma atmosphere and studied their electronic/local atomic-structure and correlated with their magnetic behaviors. Incorporation of Er³⁺-ion in ZnO-lattice [(ZnO: Er)_{sapphire/silicon}] and formation of Zn²⁺/O⁻ vacancies (V_{Zn}/V_O) at the bonding between Zn and O₂ may induces room temperature ferromagnetism. Magnetic M-H loops of pure-ZnO shows diamagnetic behaviour, whereas (ZnO: Er)_{sapphire/silicon} are ferromagnetic in nature. Moreover, (ZnO: Er)_{sapphire} is higher ferromagnetic (saturation magnetization, M_s ≈ 2.3 emu/g, coercivity, H_c ≈ 63 Oe) than (ZnO: Er)_{silicon} (M_s ≈ 0.5 emu/g, H_c ≈ 15 Oe). Incorporation of Er³⁺-ion and formation of V_{Zn}/V_O vacancies were observed from x-ray photoelectron spectroscopy (XPS) and x-ray absorption near edge structure (XANES) spectroscopy analysis. The peak positions of Zn 3p and O 1s in XPS spectrum of (ZnO: Er)_{sapphire/silicon} thin films are shifted at higher energy levels compared to pure ZnO, indicating that the behaviors of (ZnO: Er)_{sapphire/silicon} thin films are substrate dependent. XANES study of Zn K-edge/Zn L₃-edge shows the transition of Zn 1s → 4p / Zn 2p → Zn 4s3d in antibonding states of Zn; whereas Er L₃-edge is the transition of 2p → 5d states of Er upon x-ray absorption that demonstrates the local atomic structure around Er in the (ZnO: Er)_{sapphire/silicon} thin films. These transitions reveal the host-lattice in Zn-sites is substituted with Er³⁺-ions to preserve the symmetry with negligible distortion. The O K-edge shows the transition of O 2p - Zn 4s hybridized states through charge transfer the oxygen bands (Er-O-Zn) that reduced slightly atomic radius of Zn-O/Er-O/Zn-Zn found from extended x-ray absorption fine structure study, implies (ZnO: Er)_{sapphire} is higher ferromagnetic behaviour than (ZnO: Er)_{silicon}. The defect emission bands also identified through Er-substitution indicated that the emissions changed the diamagnetic-ZnO into room temperature ferromagnetic DMSs (ZnO: Er)_{sapphire/silicon} thin film that could be useful for optoelectronic/magnetic applications.

Keywords ZnO, ZnO:Er, XANES, XPS, UPS

Pure ZnO is a diamagnetic-semiconductor wide bandgap (~3.37 eV) material with high exciton binding energy (≈60 meV), enables efficient excitonic emission at room temperature that makes it most suitable material for optoelectronic applications¹⁻³. ZnO can be prepared in different forms, viz. single crystals, epitaxial films, along with various nanostructures, to meet different applications⁴. When ZnO is substituted with transition metals (TM: Fe, Co, Ni, etc.)⁵⁻⁷ and/or rare earth elements (RE: Er, Eu, Yb, etc.)⁸⁻¹¹, then ZnO can act as a 'diluted magnetic semiconductor' (DMS) materials. It is noted that the 4f- RE-metals substituted ZnO have

¹Department of Physics, Faculty of Engineering and Technology (ITER), Siksha 'O' Anusandhan Deemed to be University, Bhubaneswar 751 030, Odisha, India. ²Department of Physics, Tamkang University, Tamsui 251, Taipei, Taiwan. ³Department of Physics, CSET, University of South Africa, Florida Science Campus, Private Bag X6, Christiaan de Wet and Pioneer Avenue, Florida Park, Florida, Johannesburg 1710, South Africa. ✉email: sekharchandraray@soa.ac.in; wfpong@gms.tku.edu.tw

higher magnetic moments, compared with 3d TMs. The electrons could facilitate the ferromagnetic (FM) interaction among the RE ions as a result of the interaction between *f* electrons and host *s* electrons. Therefore, comprehending the electronic structure and magnetic characteristics of RE-substituted ZnO is crucial because of its prospective use in electronic/photo-electronic and spintronic devices. Especially, ZnO-substituted with RE erbium (ZnO: Er) can exhibit FM behaviors. The FM behaviours of ZnO: Er are often attributed to defects, like oxygen vacancies within the ZnO lattice, which can interact with the Er⁺-ions and facilitate spin alignment. Some studies report the observation of FM behaviors in ZnO: Er at room temperature. However, the exact magnetic mechanism and extent of this FM can depend on the synthesis methods, temperature, and Er⁺-concentration. In case of thin film, the magnetic behaviors are dependent not only on these parameters but also on the nature of the substrate used for the deposition of ZnO: Er thin films, as the substrate's properties can affect the film's structure, strain, defects, and ultimately, its magnetic properties. The substrate can also influence the magnetic anisotropy of the film, making it easier for the magnetization to align in a particular direction. In ZnO: Er thin films, the Er-dopant introduces magnetic moments that can interact with the surrounding ZnO matrix. The substrate can influence the interaction between Er-ions and the ZnO matrix, as whole affecting the magnetic properties of the film. The study of magnetic properties in ZnO: Er is an active research field for potential applications in electronic and spintronics due to its ability to manipulate both the charge and spin of electrons. The magnetic moment arises in Er-substituted ZnO from the localized unpaired 4*f* electrons of Er⁺-ions substituting Zn-sites in the lattice structure of ZnO. These Er⁺-ions are localized after substitution and can align with an applied magnetic field. However, the exact mechanism behind the ferromagnetism in Er-substituted ZnO is still under investigation, and achieving stable ferromagnetism at room temperature remains challenging. Among the various deposition techniques, sputtering is a potential technique, which can form thin film with strong adhesion layer¹². The quality of thin films is affected by a number of sputtering parameters, including sputtering power, substrate temperature, chamber pressure, and sputtering time¹³. Because the nature of the substrate has a significant impact on the properties of thin films, selecting the appropriate substrate is crucial in many applications because the quality of the thin film nucleation/growth behavior depends on the substrate's orientation, roughness, cleanliness, and temperature^{12–18}. The thermal expansion coefficient mismatch between a ZnO thin film and its substrate significantly impacts the thin film's quality¹⁴. Therefore, it affects the film's structural, optical, electrical and magnetic properties.

In this present study, we have grown RE element Er-substituted polycrystalline-ZnO (ZnO: Er) thin films on two different substrates, viz. sapphire and silicon [(ZnO: Er)_{sapphire/silicon}], using the DC sputtering technique. Sapphire and silicon substrates were chosen to see the crystal strain effect on deposited materials as there is a large lattice mismatch between ZnO and (ZnO: Er)_{sapphire/silicon}. These choice of substrates are also used to study the grown of the thin films on a particular orientation. Therefore, the substrate effects of sapphire and silicon on the structural, electronic/atomic, and magnetic properties of RE element Er-substituted polycrystalline-ZnO [(ZnO: Er)_{sapphire/silicon}], thin films have been studied. We have discussed several effects associated with the ZnO materials for the development of ZnO-based dilute magnetic semiconductors (DMSs) and their device-based applications. A comparative electronic/atomic/bonding-structure of (ZnO: Er)_{sapphire/silicon} thin films has been studied using X-ray absorption near edge structure (XANES) and X-ray photoelectron spectroscopy (XPS) measurements, whereas magnetic behaviors are studied using SQUID-measured magnetic hysteresis M-H loops. XANES spectroscopy is an ideal technique because it is an element-specific probe that is highly sensitive to the local structure around the absorbing crystalline and non-crystalline atoms^{19,20}. In addition, crystalline surface morphology is studied using scanning electron microscopy (SEM) images. The evolution of local electronic structures is proposed, where the Er in (ZnO: Er)_{sapphire/silicon} thin film could behave as DMSs and could be used in electronic/spintronics applications.

Results and discussion

Figure 1a,b shows the SEM micrograph of (ZnO: Er)_{sapphire/silicon} thin films. Differences in micrograph size/textures are due to the different substrate's mismatch in lattice, stress, Er-content present (at%) in the ZnO matrix, and the thermal expansion coefficient between the ZnO: Er thin film and the substrates (sapphire/silicon). From the inset Fig. 1b, a branch of leaf-shaped cone arm structure with non-uniform diameter along its axes is observed in the (ZnO: Er)_{silicon} thin film matrix, while no such structure is observed in (ZnO: Er)_{sapphire}. Zhuo et al.²¹ also observed similar four legs regular-shaped hexagonal cone arm and defined as the tetrahedral structure in nanostructures-ZnO materials. The XRD spectra of (ZnO: Er)_{sapphire/silicon} is shown in Fig. 1c,d. Different (ZnO: Er)_{sapphire/silicon} diffraction peaks and their orientations are identified/indicated in the XRD spectra^{22–26}, as shown in Fig. 1c,d. It is observed that both the films (ZnO: Er)_{sapphire/silicon} are partially oriented epitaxial polycrystalline hexagonal wurtzite structure, exhibiting (002), (111), (102), (110), (103), (004) orientations. Moreover, the XRD patterns of (ZnO: Er)_{sapphire} is grown along (111) plane; whereas (ZnO: Er)_{silicon} is grown along (002) and (111) planes. In addition, some other additional minor peaks of ZnO and the substrate (sapphire/silicon)-peaks are also observed in the respective (ZnO: Er)_{sapphire/silicon} thin films. The (ZnO: Er)_{sapphire} thin films provide better crystalline quality and surface morphology compared to (ZnO: Er)_{silicon} thin films. The silicon-substrate is a cost-effective and readily available option, especially for certain applications where UV performance is not the primary concern; whereas sapphire has a wurtzite structure, which aligns well with the wurtzite structure of ZnO film that facilitates better growth with smoother surfaces, leading better crystalline quality with reduced threading dislocations, improved crystalline orientation and larger grain sizes compared to those grown on silicon. In this context the lattice constants, crystallite size (from Scherrer's formula) and the strains are obtained from XRD analysis and tabulated in Table 1 to support crystalline quality of the (ZnO: Er)_{sapphire/silicon} thin films. It is clearly observed that the micro-strain is induced in (ZnO: Er)_{sapphire} thin film is approximately two times larger than (ZnO: Er)_{silicon} thin film which are the responsible for growing most preferentially orientation along (111) plane in case of sapphire substrate and (002), (111) plane in Si-substrate. From the obtained *c/a* values

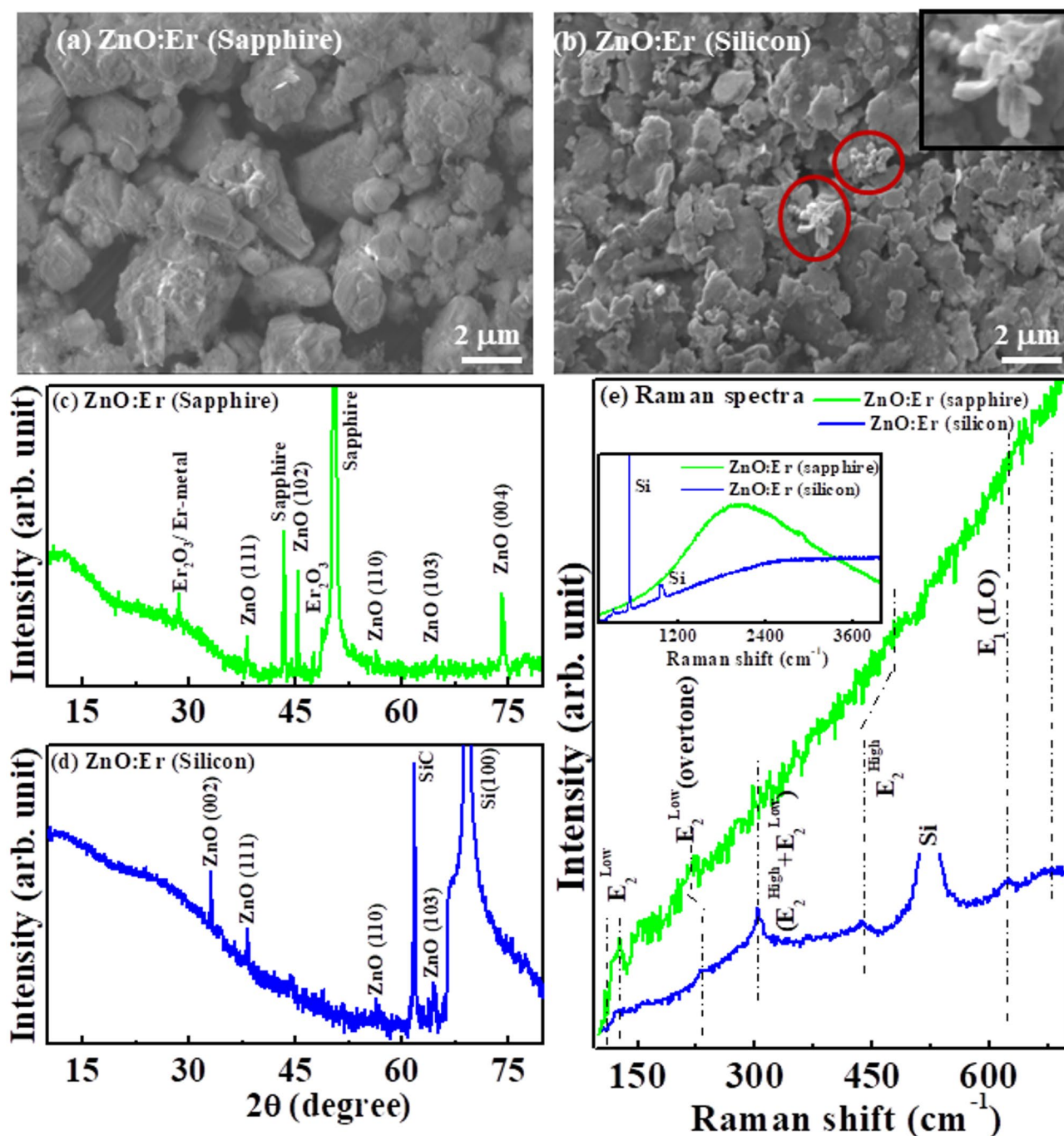


Fig. 1. (a) Scanning electron microscopy (SEM) of ZnO:Er deposited on (a) Sapphire substrate and (b) Silicon substrate. XRD patterns of ZnO:Er (c) On sapphire and (d) On silicon. Raman spectra of ZnO:Er deposited on sapphire and silicon substrate.

Sample specification	Cell parameters (Å)	<i>c/a</i>	Unit cell volume (Å ³)	Crystallite size ($t = 0.89\lambda / \beta \cos\theta$) (nm)	Strain ($\epsilon = \beta \cos\theta / 4 \sin\theta$)
ZnO:Er on sapphire substrate	$a = 3.271 \pm 0.0002$ $c = 5.132 \pm 0.0002$	1.56	47.57 ± 0.006	105 nm	1.06×10^{-3}
ZnO:Er on silicon substrate	$a = 3.270 \pm 0.001$ $c = 5.239 \pm 0.0004$	1.60	48.55 ± 0.005	93 nm	5.4×10^{-4}

Table 1. The values of cell parameters from XRD, crystallite size, strain for ZnO:Er deposited on sapphire and silicon substrate.

(see Table 1), it is observed that the ZnO structure is distorted in $(\text{ZnO:Er})_{\text{sapphire}}$ thin film compared to $(\text{ZnO:Er})_{\text{silicon}}$ thin film. It is well known that the oxide of Er i.e. Er_2O_3 exhibit anti-ferromagnetic at low temperature (~ 3.3 K) and paramagnetic at room temperature or above of 3.3 K²⁷, as a result the magnetic contribution from Er_2O_3 in this present work is ruled out. Again, the Er-cluster or Er-metal exhibits both ferromagnetic as well as paramagnetic at low temperature²⁸. As, we have not observed Er-clusters or Er-atomic cluster, so it is also ruled out in the present study. The Raman spectra of $(\text{ZnO:Er})_{\text{sapphire/silicon}}$ thin films are shown in Fig. 1e. The spectral features shows that the $(\text{ZnO:Er})_{\text{sapphire/silicon}}$ thin films are highly photoluminescence (PL) behaviours as inset Fig. 1e, while $(\text{ZnO:Er})_{\text{sapphire}}$ is higher PL than $(\text{ZnO:Er})_{\text{silicon}}$ indicating the formation of highly defective $(\text{ZnO:Er})_{\text{sapphire}}$ thin film. In a $(\text{ZnO:Er})_{\text{sapphire}}$ thin film, Raman mode peaks are difficult to observe due to the dominance of PL intensity over the Raman scattering signal. The presence of this high PL behaviour, particularly in $(\text{ZnO:Er})_{\text{sapphire}}$ thin film is due to formation higher defective thin films compare to $(\text{ZnO:Er})_{\text{silicon}}$ and responsible for the higher ferromagnetic behaviors^{29–34}. All the observed spectroscopic Raman peaks are identified in Fig. 1e can be assigned to a wurzite ZnO structure^{35–37}. However, in the Raman spectra the peak at 99 cm^{-1} is associated to the E_2 (low) dominated by the vibrations of the heavy Zn-sub-lattice and the band at around 438 cm^{-1} attributed to the E_2 (high) mode, mostly involves the oxygen atoms of $(\text{ZnO:Er})_{\text{sapphire/silicon}}$ thin film^{35–37}. A significant shift 483 cm^{-1} for the $(\text{ZnO:Er})_{\text{sapphire}}$ is observed due to the formation of different phase of ZnO:Er films. The peak 620 cm^{-1} is ascribed as the combination of optical-acoustic mode³⁸. The peak at 200 cm^{-1} is the overtone of the E_2 (low) and the peak at 336 cm^{-1} is due to the combination E_2 (high) and E_2 (low) modes^{37,38}. The E_2 (high) mode centered at 438 cm^{-1} has a stronger intensity and narrower line-width in $(\text{ZnO:Er})_{\text{silicon}}$ film, which indicates that the grown of ZnO:Er is a hexagonal wurzite structure^{37,38}.

XPS has been used to analyse the chemical composition (Zn, O, Er), quantification (at%), electronic structure and their defects. The quantificational analysis of XPS spectra shows ≈ 2.5 at% and ≈ 1.0 at% Er is substituted in $(\text{ZnO:Er})_{\text{sapphire}}$ and $(\text{ZnO:Er})_{\text{silicon}}$ thin films, respectively, although the deposition parameters/conditions remained unchanged during the deposition of $(\text{ZnO:Er})_{\text{sapphire/silicon}}$ thin films. It is also observed that the Er-content in the film structure is not only different at%, but their peak positions in Zn 3p and O 1s XPS spectra of $(\text{ZnO:Er})_{\text{sapphire/silicon}}$ as shown in Fig. 2a–d, e–h) respectively, are shifted at higher energy levels compared to pure ZnO, indicating that the deposition of ZnO:Er thin films are substrate-dependent. The corresponding Zn 3p and O 1s XPS spectra and their convolutions are shown in Fig. 2a–d and e–h, respectively. The Zn 3p spectrum for pure ZnO consists of two strong peaks at ≈ 88.4 eV and ≈ 91.5 eV, correspond to Zn $3p_{3/2}$ and Zn $3p_{1/2}$ states, respectively. The difference between the Zn $3p_{3/2}$ and Zn $3p_{1/2}$ binding energies found to be ≈ 3.1 eV, which closely matches with the value reported earlier^{39,40}. Oxygen in the ZnO matrix is coupled to Zn^{2+} ions in the + 2-oxidation state, as indicated by the locations of both peaks and the difference in their binding energies^{39,40}. The Zn 3p spectral features of $(\text{ZnO:Er})_{\text{sapphire/silicon}}$ thin films closely resemble each other with red-shift ≈ 0.8 eV [$3p_{3/2}$: ZnO (pure), 88.4 eV \rightarrow $(\text{ZnO:Er})_{\text{sapphire}}$ / $(\text{ZnO:Er})_{\text{silicon}}$, 89.5 eV/90.3 eV; $3p_{1/2}$: ZnO (pure), 91.5 eV \rightarrow $(\text{ZnO:Er})_{\text{sapphire}}$ / $(\text{ZnO:Er})_{\text{silicon}}$, 92.5 eV/93.8 eV] and increase their peak widths [ZnO \rightarrow $(\text{ZnO:Er})_{\text{sapphire}}$ \rightarrow $(\text{ZnO:Er})_{\text{silicon}}$] with variations of their intensities. This suggests that the introduction of Er influences the electronic states of Zn due to the existence of Zn interstitials/vacancies. The O 1s peak at $531.4 (\pm 0.1)$ eV of pure ZnO is believed to be due to the wurzite structure of hexagonally arranged Zn^{2+} ions in the metal oxide as

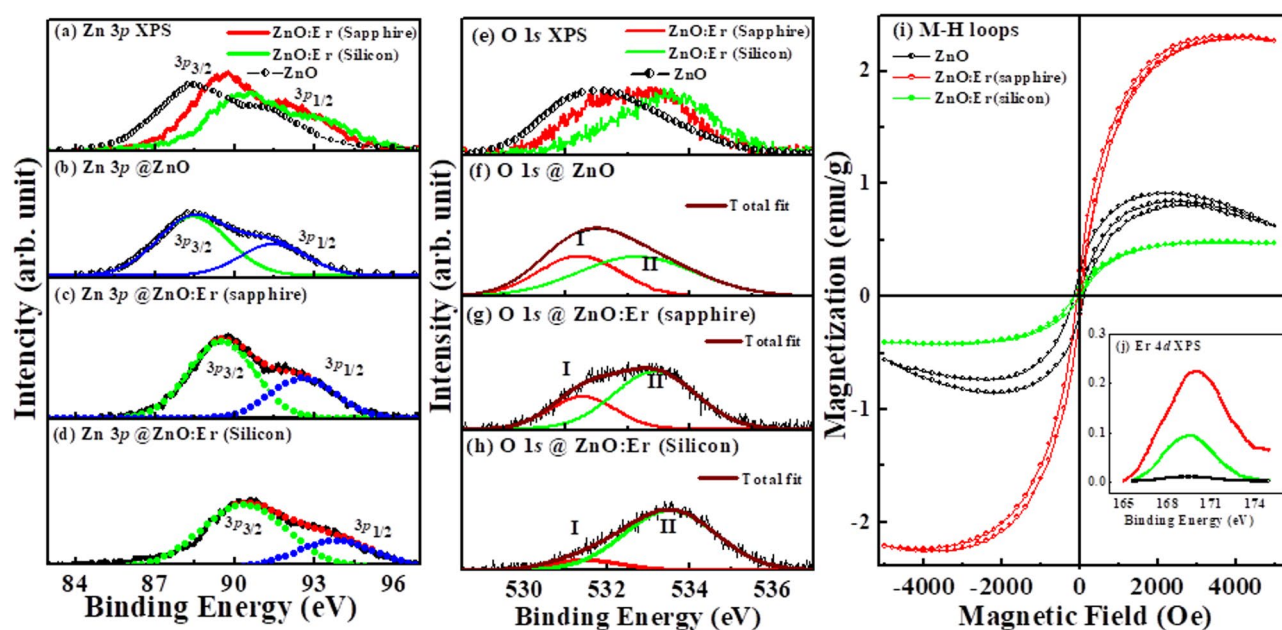


Fig. 2. (a) X-ray photoelectron spectroscopy (XPS) of (a) Zn 3p of ZnO, ZnO:Er; Zn 3p decomposed into Gaussian features (b) pure-ZnO, (c) ZnO:Er (Sapphire), (d) ZnO:Er (silicon). XPS of (e) O 1s of ZnO, ZnO:Er; O 1s decomposed into Gaussian features (f) pure-ZnO, (g) ZnO:Er (Sapphire), (h) ZnO:Er (silicon). (i) Magnetic M-H hysteresis loops of ZnO, ZnO:Er (Sapphire), and ZnO:Er (silicon). (j) Inset XPS of Er 4d.

confirmed from XRD results. Different components, such as oxygen vacancies and absorbed oxygen/hydroxyl groups^{41–43}, could be the reason for the other peak at higher binding energy, 533.0 (± 0.5) eV. Based on existing literature, it is inferred that the peak is associated with oxygen vacancies in the system^{42,43}. The incorporation of Er-ions into the ZnO lattice results in a heightened intensity of the peak at elevated binding energy, signifying an increase in oxygen vacancies. This increase in oxygen vacancies is, in turn, responsible for the improved saturation magnetization associated with Er. This implies higher room temperature ferromagnetism in (ZnO: Er)_{sapphire/silicon} thin films compared to diamagnetic ZnO. The room temperature (RT) magnetic behavioral M-H hysteresis loops of ZnO (ZnO: Er) are shown in Fig. 2i and the Er 4d XPS spectrum of (ZnO: Er)_{sapphire/silicon} thin films are shown in Fig. 2j inset in Fig. 2i. In the Er 4d XPS spectrum, the binding energy of ≈ 169.4 eV is attributed to the 4d levels of Er³⁺ ions are in a trivalent (Er³⁺) state in (ZnO: Er)_{sapphire/silicon} thin films via an interaction with an unfilled shell. Thus, we can deduce that the RT-FM is a fundamental characteristic of the materials involved by Er³⁺ ions and may be in a high-spin configuration ($4f^{11}6s^0$). While Er³⁺ ions contribute to magnetism, the mechanism is complex and often involves other factors like substitutions, carrier mediation and unpaired electron, rather than simply a high-spin configuration. In the RT magnetic M-H hysteresis loops, the contribution of the diamagnetic signals of substrates was adequately corrected. It is observed that the magnetic moment ($M_s = 2.3$ emu/g) and coercivity ($H_c = 63$ Oe) of (ZnO: Er)_{sapphire} thin film is higher than (ZnO: Er)_{silicon} thin film ($M_s = 0.5$ emu/g, $H_c = 15$ Oe) that confirms the magnetism is also substrate dependent. This observation is consistent with Er content (at %) obtained from XPS elemental/quantitative analysis, which indicates that the Er at% is substrate dependent. The (ZnO: Er)_{sapphire} has a higher Er (~ 2.5 at%), and the magnetization is also higher than the films deposited on a silicon substrate with an Er concentration of ~ 1.0 at%. In the context of Er-substitution, the predominant defects in ZnO are probably oxygen vacancies (V_o) and zinc vacancies (V_{Zn}). Specifically, V_o is expected to be more prevalent in Zn-rich environments due to its lower formation energy compared to zinc interstitials, while V_{Zn} is likely to be more prominent in oxygen-rich conditions. Thus, it is plausible to infer that there may be a significant presence of zinc and oxygen vacancies in (ZnO: Er)_{sapphire/silicon} thin films. Our experimental findings may align with the bound-magnetic-polaron (BMP) model suggested by Coey et al.⁴⁴, as the presence of both zinc and oxygen vacancies promotes the development of ferromagnetism in diluted magnetic semiconductors (DMSs)^{45,46}. It is noted that the magnetic contribution is not due to Er-oxide and/or Er-metal. As Er has more affinity towards oxygen, so oxygen deficiency occurred in parent ZnO. Higher Er-content leads to higher oxygen deficiency and forms oxygen vacancy clusters which are responsible for observation of ferro-magnetic behavior. This is the reason why we have given much emphasis on vacancy mediated ferromagnetism. According to the BMP model, magnetic exchange can be mediated by shallow donors (Zn_i) electrons that form bound magnetic polarons, and the presence of dopant, i.e., the magnetic exchange interaction between Zn or O vacancies of Er³⁺ ions occupying the same space, is aligned with Er spins³⁺, forming BMPs. With the reduction of V_o and V_{Zn} by Er-substitution in ZnO, neighboring Er-ions coupled via a V_o and V_{Zn} (ferromagnetic exchange) are connected by a zinc bond (no exchange interaction) or oxygen bond (super-exchange interaction), which are responsible for the alteration of M_s values. It is noted that the exchange interaction has not arisen due to Er. Due to high oxidation state of Er, the oxygen deficiency has been observed in the ZnO structural matrix. The exchange interaction is Er coupled and/or mediated which is responsible for the observation of ferromagnetism. The substrate can also influence the formation and characteristics of these defects, thus affecting the BMP formation and the overall magnetic behavior. In the case of (ZnO: Er)_{silicon}, the ferromagnetic behavior is weakened, possibly due to Er ions³⁺ near the surface sites with their ionic radii mismatch⁴⁷.

To investigate the electronic/atomic structures and gain insight into their microstructure, we have used the Zn and O K-edges, Zn and Er L₃-edge XANES spectra, along with Zn K-edge and Er L₃-edge EXAFS spectra of ZnO (ZnO: Er)_{sapphire/silicon} thin films. The Zn K- and O K-edges XANES spectra of ZnO (ZnO: Er)_{sapphire/silicon} thin films are shown in Fig. 3a,b. As a reference, the Zn K-edge XANES spectrum of Zn-foil (Zn⁰) is also shown in Fig. 3a. To identify the proper absorption edge, first-order differentiation of Zn K-edge XANES spectra is shown in the lower inset of Fig. 3a. The transition of Zn 1s \rightarrow Zn 4p dominates the Zn K-edge absorption spectra, which show the excited 1s core electrons of the zinc atoms. The Zn 1s \rightarrow 4p transitions are the distinctive peaks that are seen on the leading absorption edge. The fully populated 3d levels of metal Zn-atoms (Zn⁰) are pushed below the Fermi level. Nevertheless, the zinc atoms' oxides produce empty states in the 3d levels, Zn²⁺, because their electrons are required for bonding. Therefore, one might assume that an electron excited from the core levels would have a d-level state. However, quantum selection criteria, which prohibit s electrons from moving in d shells (i.e., $\Delta l = \pm 1$) prevent the 1s \rightarrow 3d transition. The Zn K-edge absorption edge of Zn-foil (Zn⁰) and pure-ZnO are observed at ≈ 9659.1 eV and ≈ 9665.5 eV respectively, along with a weak pre-edge at ≈ 9657.0 eV (marked with a black line), which are the hybridization of O-2p and Zn²⁺ 3d orbitals⁴⁸. The ZnO exhibits molecular bands characterized by narrower 4p levels, with the closest neighbouring atoms being oxygen. The outer-shell electrons of the oxygen atoms are confined to the 2p levels, while the unoccupied levels on the zinc atoms correspond to the 4p levels. Quantum selection rules arise due to an interaction between the p-levels, which results in the narrowing of the 4p levels in ZnO materials (i.e. Zn²⁺). The absorption edges of Er-substituted ZnO, (ZnO: Er)_{sapphire/silicon} are observed at ≈ 9663.0 eV/9662.5 eV, in between Zn-foil and pure ZnO as shown in the upper inset of Fig. 3a. The edge shifts from ≈ 9665.5 eV (ZnO) \rightarrow ≈ 9663.0 eV/9662.5 eV (ZnO: Er)_{silicon/sapphire} thin films indicate the oxidation states of ZnO: Er (between Zn²⁺ and Zn⁰) are decreased on (ZnO: Er)_{silicon/sapphire} thin films compared to pure ZnO. The oxidation states of (ZnO: Er)_{sapphire} thin film is nearer to Zn-foil (Zn⁰) than (ZnO: Er)_{silicon}, due to the edge shift being ≈ 0.5 eV lower than (ZnO: Er)_{silicon}. It is also noticed that the pre-edge of Er-substituted ZnO is merged with the absorption edge in both (ZnO: Er)_{sapphire/silicon} films. Similar edge shifts are also observed in O K-edge XANES spectra, illustrate in the upper inset Fig. 3b, provide a magnified perspectives of the pre-edge characteristics following the subtraction of the background as lower inset Fig. 3b, which has been accomplished using a best-fitted Gaussian curve as denoted by the dotted line. This variation in

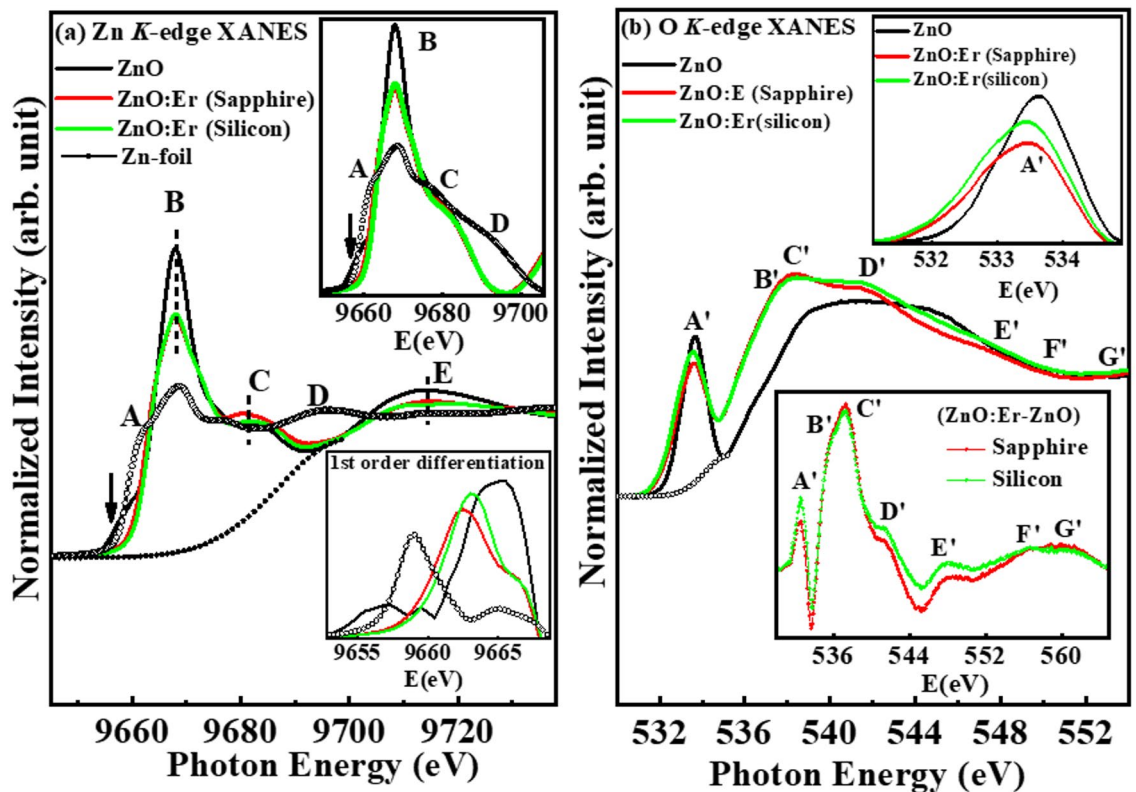


Fig. 3. (a) Zn *K*-edge X-ray absorption near edge structure (XANES) spectra of ZnO and ZnO: Er deposited on sapphire/silicon substrate. The lower inset displays the 1st order differentiation of the Zn *K*-edge XANES spectra and upper inset display a magnified view of the pre-edge features after the background has been subtracted using a best-fitted Gaussian line. (b) O *K*-edge XANES spectra of ZnO and ZnO: Er deposited on sapphire/silicon substrate. The upper inset displays a magnified view of the pre-edge features after the background has been subtracted using a best-fitted Gaussian line, whereas the lower inset plots differences of O *K*-edge between ZnO: Er and ZnO (ZnO: Er-ZnO).

the general line shapes, the absorption intensity, and the positions of the peaks of the Zn and O *K*-edge XANES spectra, as shown in Fig. 3a, b of the pure-ZnO and (ZnO: Er)_{sapphire/silicon} has been regarded as evidence of substrate-dependent in O/Zn-*p* states. According to the dipole-transition selection rule, features A, B, C, and D, as shown in Fig. 3a, can be attributed to the Zn 4*p*-derived state. In Zn *K*-edge, the main feature at ≈ 9668.0 eV (marked as B) is attributed to the Zn-atoms in tetrahedral site symmetry of ZnO⁴⁹. The upper inset of Fig. 3a shows a comparison of Zn *K*-edge spectra of ZnO and (ZnO: Er)_{sapphire/silicon} thin films. A detailed view of the near-edge characteristics following the subtraction of the background, which has been accomplished using a best-fitted Gaussian curve as represented by the dotted line. No pre-edge feature is observed in (ZnO: Er)_{sapphire/silicon}, but peak shifts occur on the (ZnO: Er)_{sapphire/silicon} thin films. The peaks at $\approx 9683/9712$ eV (marked as C/D) of ZnO/(ZnO: Er)_{silicon} films because of the diverse scattering effects of the photoelectrons in the neighboring atoms environment that shifted to $\approx 9681/9714$ eV for the (ZnO: Er)_{sapphire} films. We have obtained the intensities by integrating the area within the range 9648.5–9595.5 eV for ZnO, 9653.0–9697.0 eV for (ZnO: Er)_{sapphire/silicon} thin film and found that the intensity of ZnO: Er is reduces from ZnO (29 unit) \rightarrow ZnO: Er (sapphire/silicon): 25.5/25.3 unit). Again, the intensity of (ZnO: Er)_{sapphire} films is higher than the films (ZnO: Er)_{silicon}, which implies an increase of the Zn 4*p*-orbital occupation or the positive effective charge on the Zn-ions that supports the formation of higher ferromagnetic behavior in ZnO: Er thin films. Figure 3b shows O *K*-edge XANES spectra of ZnO/(ZnO: Er)_{sapphire/silicon}. In accordance with the dipole-transition selection rule, the distinct peaks observed in the energy range 531–565 eV originate from O 1*s*-derived states transitioning to 2*p* _{σ} -derived (along the bilayer) and O 2*p* _{π} -derived (along the *c* axis) states^{50–52}. The contributions in the absorption edge mainly arise from O 2*p* - Zn 4*s* hybridized states⁵³. The strong features A is due to the asymmetry of the wurtzite structure. The absorption edges are shifted to lower energy, when Er is substituted with ZnO, which can be seen in an enlarged depiction of the pre-edge (feature-A') after the background has been eliminated, utilizing a best-fitted Gaussian curve as indicated by the dotted line as shown in the upper inset of Fig. 3b. The fact that the intensity of (ZnO: Er)_{sapphire/silicon} thin films (feature-A') was found to be lower than pure ZnO (upper inset Fig. 3b) indicating the total number of unoccupied O 2*p*-derived states is decreased, which can be seen as the transfer of electrons from Er \rightarrow O 2*p* states due to O 2*p*-Er 5*d* hybridizations in (ZnO: Er)_{sapphire/silicon} thin films^{50,51}. The lower inset Fig. 3b shows the differences in the O *K*-edge near edge features of [(ZnO: Er)_{sapphire/silicon} - (ZnO)] thin films. The overall spectral intensity of (ZnO: Er)_{sapphire/silicon} has been reduced and the near-edge feature

has been broadened in comparison to those of ZnO, indicating a reduction in the number of unoccupied O 2p states because of the Er-diffusion and heightened negative effective charge of the O ion. The rise in the effective charge of the O ions is explained by the observation that Pauling's electronegativity of Er (1.24) is considerably less than that of Zn (1.65)⁵⁴. The enhancement of these characteristic features (A', B', C', D', E', F', G') signifies the elevated local density of states (DOS) that originate from the defects and/or dangling bonds present in ZnO/(ZnO: Er)_{sapphire/silicon} thin films⁵⁵. Again, intensities of the features B', C', G' is higher in (ZnO: Er)_{sapphire} thin films compared to (ZnO: Er)_{silicon} films; whereas the features A', D', E', F' of the (ZnO: Er)_{silicon} films is higher than (ZnO: Er)_{sapphire} films, indicating the population of defects and/or vacancies are substrate dependent. The overall intensities of (ZnO: Er)_{sapphire} film is lower than (ZnO: Er)_{silicon} suggesting a rise in the occupancy of the O 2p orbitals and an increase in the negative effective charge of the O-ion that supports the higher ferromagnetism in the (ZnO: Er)_{sapphire} films.

Figure 4a,b shows Zn L_3 -edge and Er L_3 -edge XANES spectra of ZnO and (ZnO: Er)_{sapphire/silicon} thin films. XANES measurements examine the Zn L -edge, providing knowledge of the unoccupied Zn d and Zn s -states. The Zn L_3 and L_2 regions, correspond to the Zn $2p \rightarrow Zn 4s$ and Zn $2p \rightarrow Zn 3d$ anti-bonding states, respectively⁵⁶. The spectral characteristics observed in the L_2 region indicate the electron transition from Zn $2p$ state to Zn $3d$ state. No pre-edge feature is observed in ZnO/(ZnO: Er)_{sapphire/silicon} implying no Zn $4s$ band transition occurs. The Zn L_3 -edge absorption peaks arise due to the transition of the $2p$ core electron to the unoccupied $4s/4d$ levels as final states. In accordance with the dipole-transition selection rule, Zn L_3 -edge XANES investigates the unoccupied states derived from Zn s - and d -orbitals. The Zn- $3d$ orbital is completely filled, making the lowest unoccupied orbital of the Zn-ion is Zn- $4s$, succeeded by Zn- $4p$ and Zn- $4d$ ⁵⁷. The degenerate states $2p_{3/2}$ and $2p_{1/2}$ emerge due to spin-orbit coupling, leading to multiplets centered at ≈ 1027.8 eV and ≈ 1032.0 eV. The crystal field (octahedral) raises the degeneracy of $2p_{3/2}$ and $2p_{1/2}$ levels, creating of t_{2g} and e_g sub-band symmetries⁵⁸. The fine structure multiplets arise from two effects: (i) interaction between the $3d$ (electron) and $2p$ core hole, and (ii) crystal field created by neighboring ions at a Zn²⁺ site⁵⁹. The inset at the bottom of Fig. 4a is a magnified view of the near-edge features after subtracting the background using a best-fitted Gaussian curve indicated by the dotted line. It is found that the absorption features A/B(wide range) are observed at $\approx 1027.8/1031.9$ eV in ZnO, which is shifted towards lower energy level (A'/B') at $\approx 1027.3/1028.9$ eV for the (ZnO: Er)_{sapphire} film and $\approx 1027.3/1029.0$ eV in (ZnO: Er)_{silicon} film, respectively. The overall peak width and intensities of (ZnO: Er)_{sapphire/silicon} thin films are decreased compared to pure-ZnO, indicating that the quantity of unoccupied Zn $4sd$ states in proximity to the conduction-band minimum is lowered as the Er is substituted with ZnO. We have integrated the Zn L_3 -edge region and found that the intensity of pure ZnO ≈ 0.77 (a.u.) is

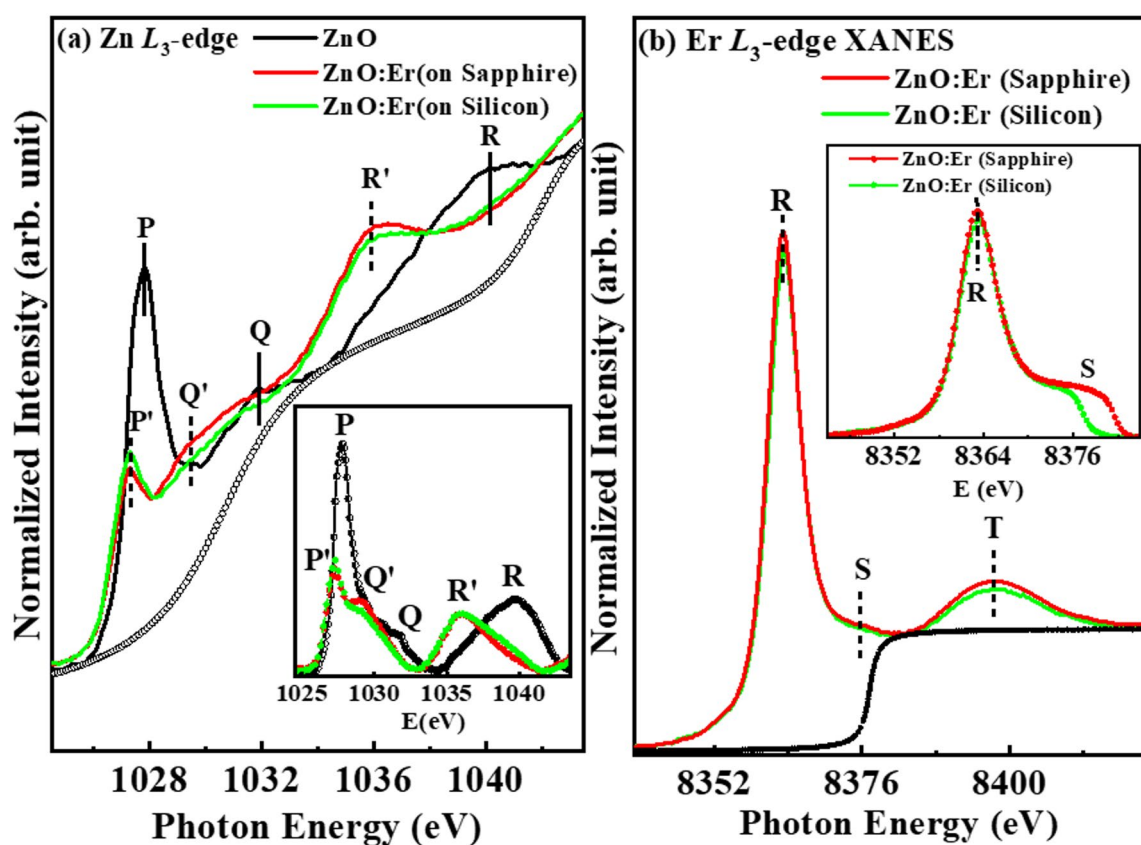


Fig. 4. (a) Zn L_3 -edge and (b) Er L_3 -edge X-ray absorption near edge structure (XANES) spectra of ZnO and ZnO: Er deposited on sapphire/silicon substrate. Inset (a, b) display a magnified view of the Zn L_3 and Er L_3 pre-edge features after the background has been subtracted using a best-fitted Gaussian line.

higher relative to $(\text{ZnO: Er})_{\text{sapphire/silicon}} \approx 0.49/0.47$ (a.u.). The intensity of $(\text{ZnO: Er})_{\text{sapphire}}$ films higher than the $(\text{ZnO: Er})_{\text{silicon}}$, indicating that the unoccupied Zn 4*s*d states are higher in $(\text{ZnO: Er})_{\text{sapphire}}$ than $(\text{ZnO: Er})_{\text{silicon}}$. The augmentation of the defining features denotes the heightened local density of states (DOS) that originate from defects or dangling bonds within various ZnO nanostructures⁵¹. The $(\text{ZnO: Er})_{\text{sapphire}}$ thin film shows higher absorption intensity concerning the $(\text{ZnO: Er})_{\text{silicon}}$ thin film, signifying a greater prevalence of defects and/or vacancies at O sites in $(\text{ZnO: Er})_{\text{sapphire}}$ thin film. As a result, the ferromagnetic nature is stronger in the $(\text{ZnO: Er})_{\text{sapphire}}$ thin film than $(\text{ZnO: Er})_{\text{silicon}}$. To investigate the local electronic structure of Er in ZnO, we used the XANES spectrum of Er-substituted ZnO at Er L_3 -edge. The variation of white line intensity of $(\text{ZnO: Er})_{\text{sapphire/silicon}}$ thin films is at ≈ 8363.3 eV and ≈ 8398.0 eV respectively, as shown in Fig. 4b. The peaks at ≈ 8363.3 eV (R) and ≈ 8398.0 eV (T) arise due to the $2p-5d$ transition of Er upon x-ray absorption^{60–66}. The magnitude of the white line peak signifies the occupancy of $5d$ valence electronic states, which is contingent upon the symmetry of the absorbing atom. A high-order symmetry, such as that of the ErO_6 octahedron (O_h point group), results in a concentrated density of states (DOS) of the $5d$ states, attributed to the equivalent coordination of six O atoms around Er. This concentrated DOS leads to a significant pre-edge peak; nevertheless, the peak height of the $(\text{ZnO: Er})_{\text{silicon}}$ thin film is reduced as a result symmetry degradation⁵⁹. The observed decrease in intensity to a reduced DOS concentration, which can be ascribed to the less symmetric geometry in the coordination^{53,58}. Thus, the symmetry around Er increases for the $(\text{ZnO: Er})_{\text{sapphire}}$ thin film as shown in the inset lower of Fig. 4b, implying the higher DOS. This higher DOS ($2p-5d$) of $(\text{ZnO: Er})_{\text{sapphire}}$ thin film implies a higher ferromagnetic nature compared to the $(\text{ZnO: Er})_{\text{silicon}}$ film.

The best tool for further study of the local structure around Zn atoms in Er-substituted ZnO is extended x-ray absorption fine structure (EXAFS) spectroscopy. The oscillations observed in EXAFS arise from the scattering and interference of photoelectron waves from source atoms with elevated kinetic energies. Due to their kinetic energy, photoelectrons can move between adjacent atoms. The outer shell electrons of these neighboring atoms exert a coulombic force on the incoming photoelectrons, which then follow a path characterized as either single or multiple scattering. The fluctuation EXAFS spectra can be extracted by using the ATHENA and ARTEMIS programs.⁶⁷ In this case, Fourier transform of $k^3\chi$ was performed, where k is the photoelectron wave vector, defined as $k = (4\pi m (E - E_0)/h)^{1/2}$, where m is the electron mass, E is the photon energy, E_0 is the energy threshold of the absorption edge, and h is the Planck constant. This Fourier transform gives the radial structural function (RSF) around Er i.e., the atomic distribution. This involves the reduction of data from the absorption spectra and the use of Fourier transform to obtain the $\chi(R)$ versus R plots, the development of theoretical EXAFS spectra starting from a hypothesized crystallographic structure, and finally the fitting of the experimental $\chi(R)$ versus R data with the theoretical data using the ARTEMIS programs⁶⁷. The fitting parameters consist of the coordination number (N), bond distances, and disorder (Debye-Waller) factors (σ^2), which indicate the mean square fluctuations in the distances. To analyze the local structure around Zn and Er in detail, $\chi(R)$ versus R plots generated for ZnO and $(\text{ZnO: Er})_{\text{sapphire/silicon}}$ thin films from the $\mu(E)$ versus E spectra through the Fourier transform of the $\chi(k)$ versus k plots with appropriate $k(k^3)$ weighting are presented in Fig. 5, measured at the Zn K -edge and Er L_3 -edge. Figures 5a,b illustrate the amplitude of the Fourier transform (FT) obtained from the EXAFS $k^3\chi$ data for ZnO and $(\text{ZnO: Er})_{\text{sapphire/silicon}}$ films, along with Zn-Foil as reference, and their respective oscillations at the Zn K -edge. The peak observed in Zn-foil at ≈ 2.58 Å is described as a Zn-Zn bond, and the peak at ≈ 1.84 Å observed in pure ZnO is defined as Zn-O coordination bond. It shows that the line shapes and radial distribution of the FT spectra at Zn K -edge of the Er-substituted ZnO are not identical to ZnO, but with a slight change in their intensities and peak positions. The Zn-O bond lengths of ZnO: Er films are reduced to ≈ 1.63 Å/1.87 Å (sapphire/silicon-substrate) compared to pure ZnO films (≈ 1.84 Å), but the Zn-Zn bond length increased to 3.09 Å/3.16 Å [$(\text{ZnO: Er})_{\text{sapphire}}/(\text{ZnO: Er})_{\text{silicon}}$] compared to Zn-foil (≈ 2.58 Å)⁴⁸. In addition, one extra peak at ≈ 1.35 Å is observed in $(\text{ZnO: Er})_{\text{silicon}}$ films, equivalent to the weak peak at ≈ 1.15 Å observed in pure ZnO films and also defined as the Zn-O bond⁵⁹. These results suggest that the Er-atoms take the place of the host Zn ions in the core of ZnO: Er; the local atomic configuration at the Zn sites is markedly distorted, owing to the substantial difference in ionic radii of Er^{3+} (0.89 Å) and Zn^{2+} (0.74 Å). It is considered that the Er atoms substituted at the Zn sites on the surface layer and formed dangling bonds/defects with a high degree of disorder. The EXAFS $k^3\chi$ data as shown in Fig. 5b indicates the spectral features of $(\text{ZnO: Er})_{\text{silicon}}$ film is identical with pure ZnO but non-identical with $(\text{ZnO: Er})_{\text{sapphire}}$ film indicates along with a slight phase shift in scattering data beyond $k = 6$ Å⁻¹. This indicates a minor disturbance on the formations at closer distance to the source Zn atoms in $(\text{ZnO: Er})_{\text{sapphire/silicon}}$ thin films. An observable shift at the Zn-O bond peak position points out a disturbance in the atomic locations. It is highlighted a displacement of defects in $(\text{ZnO: Er})_{\text{sapphire/silicon}}$ compared to the host elements of the ZnO materials in their wurtzite crystal structure with Er-substitution. These disorders and/or defects are higher in $(\text{ZnO: Er})_{\text{sapphire}}$ thin film, implying higher ferromagnetic behaviors. Figure 5c shows the radial structure function of $(\text{ZnO: Er})_{\text{sapphire/silicon}}$ and Fig. 5d is the k^3 -weighted EXAFS spectra of $(\text{ZnO: Er})_{\text{sapphire/silicon}}$. In EXAFS, the peak between 1.4 Å and 2.2 Å is the contribution of oxygen atoms in the ZnO: Er system⁵⁷. The nearest-neighbor atom from Er is found at ≈ 1.7 Å/1.84 Å [$(\text{ZnO: Er})_{\text{sapphire}}/(\text{ZnO: Er})_{\text{silicon}}$] consistent with the observations reported by other groups⁶¹, where they found that the first neighbor atom should be O. In addition, a shoulder peak at ≈ 2.4 Å was observed near the first nearest-neighbor peak in $(\text{ZnO: Er})_{\text{sapphire}}$ films, suggesting the structural distortion of pseudo-octahedral^{55,60}, implying the formation of higher ferromagnetic nature. The Fourier transformed (FT) $\chi(k)$ with k weight as shown in Fig. 5d, gives a pseudo-radial structure function around Er⁵⁹. In this, a slight phase shift in scattering data beyond $k = 6$ Å⁻¹ indicates a slight disturbance of the atoms closer to the source Zn atoms in $(\text{ZnO: Er})_{\text{sapphire/silicon}}$ thin film.

In conclusion, the DC sputtering method successfully synthesized the pure ZnO and $(\text{ZnO: Er})_{\text{sapphire/silicon}}$ thin films. ZnO was crystallized in the hexagonal wurtzite structure of ZnO without any impurity phases. The most common defects in ZnO/ $(\text{ZnO: Er})_{\text{sapphire/silicon}}$ thin films are $V_{\text{O}}/V_{\text{Zn}}$ vacancies, which are confirmed from the transitions of Zn $1s \rightarrow 4p$, Zn $2p \rightarrow 4s$, Zn $2p \rightarrow 3d$, and O $1s \rightarrow 2p$ in XANES study and peak shifts

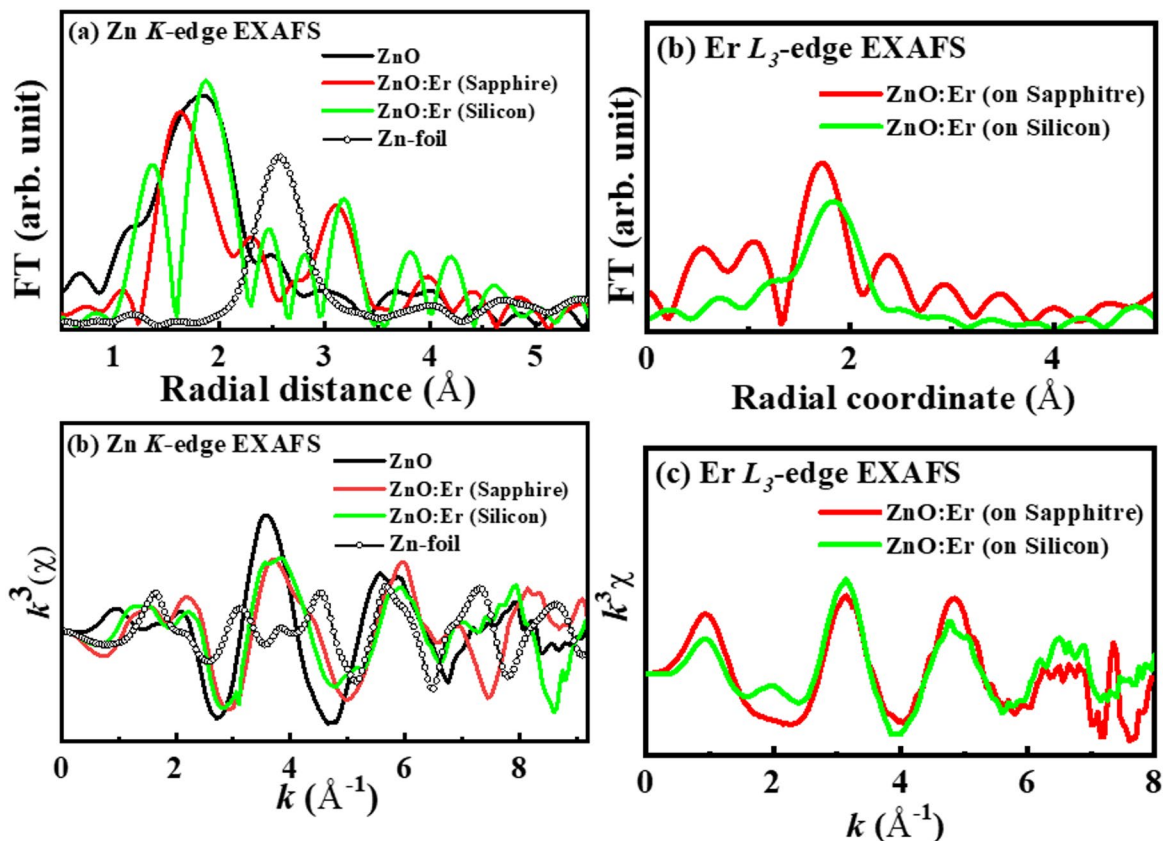


Fig. 5. Magnitude of Fourier transform (FT) of EXAFS $k^3\chi$ data at the (a) Zn K -edge and (b) Er L_3 -edge and (c, d) corresponding EXAFS data within the range $k=0$ to 8 \AA^{-1} , weighted by ZnO and ZnO:Er deposited on sapphire/silicon substrate along with Zn-Foil.

of Zn $2p$ /O $1s$ at higher binding energy level in XPS study. In XANES study, transitions occurred with the hybridization of O $2p_{\sigma}$ and O $2p_{\pi}$ -derived states. These transitions/hybridizations in (ZnO:Er)_{sapphire/silicon} thin films are lower than pure ZnO due to Er-substitution with ZnO, which implies the existence of zinc/oxygen vacancies in the (ZnO:Er)_{sapphire/silicon} thin films. The Er-ions are in trivalent states in ZnO:Er thin films, and the ferromagnetism is caused by the substitution of Zn^{2+} in the ZnO lattice by Er^{3+} -ions. Results shows that the magnetic moment in (ZnO:Er)_{sapphire} is higher than (ZnO:Er)_{silicon} thin film due to more Er^{3+} -ions occupying adjacent cation lattice positions. With the reduction of oxygen vacancies by Er-substitution in ZnO, neighboring Er-ions coupled *via* oxygen vacancy/bonds (ferromagnetic exchange/super-exchange interaction) are coupled in (ZnO:Er)_{sapphire}, which are responsible for the higher value of M_s . The overall occupying of Er^{3+} -ions due to higher vacancies/hybridization in (ZnO:Er)_{sapphire} thin film, provides the higher ferromagnetic signals at room temperature as observed in magnetic M-H hysteresis loops, where the magnetic parameters M_s/H_c in (ZnO:Er)_{sapphire} films is greater than the (ZnO:Er)_{silicon} films. These (ZnO:Er)_{sapphire/silicon} thin film DMSs could be employed for optoelectronic as well as spintronic applications.

Methods

Preparation of ZnO and Er-substituted ZnO

ZnO and Er-ZnO thin films were grown using the DC sputtering technique using sapphire and silicon substrates, respectively. Highly dense ZnO and Er-substituted ZnO ($\text{Zn}_{0.95}\text{Er}_{0.05}\text{O}$) targets of size 2.5 cm diameter and 0.5 cm thickness were prepared by solid state reaction technique. The targets were sintered at $650 \text{ }^\circ\text{C}$ for 5 h to have higher densification. These targets were used in DC sputtering unit. The sputtering chamber was evacuated with high purity Ar and then O_2 separately to remove the unwanted volatile impurities present within the chamber. The sputtering was carried out using a plasmagen gas mixture of argon and oxygen with a percentage ratio of 70:30 and the chamber pressure was kept at $\sim 10^{-6}$ Torr. The sputtering power was fixed at maximum of 100 W. The silicon and sapphire substrates were used for depositing ZnO and Er-substituted ZnO over it. Initially the substrates were ultrasonically cleaned using acetone, isopropanol, HF and mixture of HNO_3 & H_2SO_4 , stepwise. Finally, the substrates were cleaned using potassium dichromate and isopropanol. Once the substrate was cleaned, it was fixed in the substrate holder present in the sputtering unit. The substrate temperature was kept at $700 \text{ }^\circ\text{C}$ during deposition and later annealed at the same temperature to improve the oxygen content with a heating and cooling rate of $5 \text{ }^\circ\text{C}/\text{min}$.

Characterization

The surface morphology and microstructure were investigated by scanning electron microscopy (SEM) (Philips, XL30). The crystal structure was analyzed with Rigaku Miniflex XRD in the Bragg diffraction angle of 10° to 80° using CuK_α radiation source ($\lambda = 1.5404 \text{ \AA}$) at 40 KV and 15 mA. Raman spectra were measured using HORIBA scientific XploRA at 532 nm (2.41 eV) LASER light excitation energy. Magnetic properties of ZnO:Er are typically measured using techniques like the superconducting quantum interference device (SQUID) to analyses magnetization curves. The Zn K -edge and Er L_{3-} -edge XANES measurements were taken at the Wiggler-17C1 beamline; whereas Zn L_{3-} edge and O K -edge XANES measurements were taken at the 20A1 beamlines, and XPS measurements were taken from TLS-09A1 beamlines of Taiwan Light Source at the National Synchrotron Radiation Research Center (NSRRC) in Hsinchu, Taiwan. The Zn K -edge EXAFS spectra were obtained in fluorescence mode, while the O K -edge and Zr/Zn L_{3-} -edge spectra were obtained in surface-sensitive electron-yield mode. The resolution was set to 0.1 eV (0.2 eV) at a photon energy of 530 eV (1020 eV) for the O K -edge (Zn L_{3-} -edge) XANES measurements. All XANES measurements were carried out to study the electronic structures of ZnO:Er thin films deposited on sapphire and silicon substrates. Zn K -edge and Er L_{3-} -edge EXAFS were performed to investigate the local structure of Er in ZnO:Er thin films.

Data availability

All data generated or analysed during this study are included in this manuscript files.

Received: 15 July 2025; Accepted: 16 October 2025

Published online: 20 November 2025

References

1. Moon, T. H. et al. The fabrication and characterization of ZnO UV detector. *Appl. Surf. Sci.* **240**, 280–285 (2005).
2. Sucheta, M. et al. ZnO transparent thin films for gas sensor applications. *Thin Solid Films*. **515**, 551–554 (2006).
3. Choi, B. J. et al. Influence of substrate on the nucleation and growth behaviors of $\text{Ge}_2\text{Sb}_2\text{Te}_5$ films by combined plasma enhanced atomic layer and chemical vapour deposition. *Chem. Mater.* **21**, 2386–2396 (2009).
4. Morkoç, H. et al. *Zinc Oxide: Fundamentals, Materials and Device Technology* (Wiley-VCH Verlag GmbH & Co. KGaA, 2009).
5. Lee, H. J. et al. Study of diluted magnetic semiconductor: Co-Substituted ZnO. *Appl. Phys. Lett.* **81**, 4020–4022 (2002).
6. Jabbar, I. et al. Diluted magnetic semiconductor properties in TM substituted ZnO nanoparticles. *RSC Adv.* **12**, 13456–13456 (2022).
7. Li, Q. et al. Robust ferromagnetism of (Co, Er) co-implanted ZnO-based diluted magnetic semiconductor. *J. Alloys Compd.* **918**, 165749 (2022).
8. Poorapakash, B. et al. Robust ferromagnetism of ZnO:(Ni+Er) diluted magnetic semiconductor nanoparticles for spintronic applications. *Cer. Inter.* **47**, 18557–18564 (2021).
9. Qi, J. et al. Magnetic properties of Er-substituted ZnO films prepared by reactive Magnetron sputtering. *Appl. Phys. A.* **100**, 79–82 (2010).
10. Jayachandiraiah, C. et al. Erbium Induced Magnetic Properties of Er/ZnO Nanoparticles. *DAE Solid State Physics Symposium AIP Conf. Proc.* 1731, 050116: 1–4 (2015).
11. Zhang, J. et al. Synthesis and magnetic properties of Zr substituted ZnO nanoparticles. *Nanoscale Res. Lett.* **6**, 587:1–7 (2011).
12. Ohmukai, M. et al. ZnO films deposited on glass by means of DC sputtering. *J. Mater. Sc Chem. Eng.* **4**, 1–7 (2016).
13. Puthiyottill, H. et al. Exploring the effects of substrate and substrate temperature on the properties of radio frequency Magnetron sputtered ZnO thin films. *Mater. Today Commun.* **36**, 106455 (2023).
14. Lee, J. B. et al. Effects of lattice mismatches in ZnO/substrate structure on the orientation of ZnO films and characteristics of SAE devices. *Thin Solid Films*. **447–448**, 296–301 (2004).
15. Gao, K. et al. Influences of substrate and annealing on the structural and optical properties and photoluminescence of nanocrystalline ZnO films prepared by plasma-assisted pulsed laser deposition. *J. Phys. Chem. C.* **44**, 19139–19144 (2009).
16. Zhu, X. et al. Influence of the substrate on structural, morphological and optical properties of TiO_2 thin films deposited by reactive Magnetron sputtering. *AIP Adv.* **7**, 125326:1–8 (2017).
17. Ianno, N. J. et al. Characterization of pulsed laser deposited ZnO. *Thin Solid Films*. **220**, 92–99 (1992).
18. Ilyas, U. et al. Oxygen-rich-p-type ZnO thin films using a wet chemical route with enhanced carrier concentration by temperature-dependent tuning of acceptor defects. *J. Appl. Phys.* **110**, 093522:1–8 (2011).
19. Waychunas, G. A. et al. Surface complexation and precipitate geometry for aqueous Zn(II) sorption on ferrihydrite: II. XANES analysis and simulation. *Geochim. Et Cosmochim. Acta.* **67**, 1031–1043 (2003).
20. Ressler, T. et al. Quantitative speciation of Mn-Bearing particulates emitted from autos burning (Methylcyclopentadienyl) manganese Tricarbonyl-Added gasolines using XANES spectroscopy. *Environ. Sci. Technol.* **34**, 950–958 (2000).
21. Zhuo, R. F. et al. Morphology-controlled synthesis, growth mechanism, optical and microwave absorption properties of ZnO nanocombs. *J. Phys. D: Appl. Phys.* **41**, 185405 (2008).
22. Kalpanaa, V. N. et al. Biosynthesis of zinc oxide nanoparticles using culture filtrates of *Aspergillus niger*: Antimicrobial textiles and dye degradation studies. *OpenNano* **3**, 48–55 (2018).
23. Kandasamy, B. et al. Strontium-supported erbium oxide nanoparticles for efficient organic pollutant degradation under UV-Visible light. *J. Mater. Sc : Mater. Electron* **33**, 20384–20398 (2022).
24. Mohankumar, M. et al. XRD peak profile analysis SiC reinforced Al_2O_3 Ceramic Composite Synthesis by electrical resistance heating and microwave sintering: A comparison. *Adv. Mater. Sci. Eng.* **2021**, 8341924 (2021).
25. Kim, J. et al. Low-Temperature epitaxial growth of AlN thin films on a mo Electrode/Sapphire substrate using reactive sputtering. *Coatings* **11**, 443:1–9 (2021).
26. Singh, S. K. et al. Micro-structure and ferroelectric properties of BiFeO_3 thin films formed on Pt-coated r-plane Sapphire substrates. *J. Electroceram.* **16**, 553–556 (2006).
27. Moon, R. M. Magnetic structure of Er_2O_3 and Yb_2O_3 . *J. Appl. Phys.* **38/3**, 1383 (1967).
28. Frazer, H. et al. Magnetic phase diagrams of erbium. *J. Appl. Phys.* **85/8**, 6100–6102 (1999).
29. Amami, P. E. Cr doped zno: investigation of magnetic behaviour through SQUID and ESR studies. *Phys. B: Condens. Matter.* **572**, 60–65 (2019).
30. Routray, U. et al. Origin of magnetism probed through electron spin resonance studies in $\text{Zn}_{1-x}\text{Mn}_x\text{O}$ synthesized by chemical route. *Mater. Chem. Phys.* **213**, 52–55 (2018).
31. Ghosh, B. et al. Defect induced room temperature ferromagnetism in single crystal, Poly-crystal and Nanorod zno: A comparative study. *J. Appl. Phys.* **123**, 161507:1–9 (2018).

32. Mishra, D. K. et al. Signature of magnetization in Xe ions implanted ZnO: correlation with oxygen defects as probed by photoelectron spectroscopy. *J. Nanosci. Nanotechnol.* **17**, 8494–8499 (2017).
33. Routray, U. et al. Temperature-dependent ferromagnetic behavior in nanocrystalline ZnO synthesized by pyrophoric technique. *Mater. Lett.* **137**, 29–31 (2014).
34. Mishra, D. K. et al. Effect of 1.2 MeV argon ions irradiation on magnetic properties of ZnO. *Appl. Surf. Sci.* **282**, 954–959 (2013).
35. Umar, A. et al. Non-catalytic growth of high aspect-ratio ZnO nanowires by thermal evaporation. *Solid State Commun.* **139**, 447–451 (2006).
36. Lin, X. X. et al. Synthesis and optical and magnetic properties of diluted magnetic Semiconductor Zn_{1-x}MnxO Hollow spherical structures. *J. Phys. Chem. C.* **113**, 1812 (2009).
37. Russo, V. et al. Multi-wavelength Raman scattering of nanostructured Al-substituted zinc oxide. *Appl. Phys.* **115**, 073508 (2014).
38. Armelao, L. et al. ZnO:Er (III) nanosystems analyzed by XPS. *Surf. Sci. Spect.* **13**, 9–16 (2006).
39. Senapati, S. et al. Designing dual emissions via Co-doping or physical mixing of individually substituted ZnO and their implications in optical thermometry. *ACS Appl. Mater. Interfaces.* **9**, 16305–16312 (2017).
40. Gaggiotti, G. et al. Surface chemistry of Tin oxide-based gas sensors. *J. Appl. Phys.* **76**, 4467–4471 (1994).
41. Li, F. et al. Strong correlation between oxygen vacancy and ferromagnetism in Yb-substituted ZnO thin films. *J. Appl. Phys.* **116**, 243910:1–6 (2014).
42. Wei, X. Q. et al. Blue luminescent centers and microstructural evaluation by XPS and Raman in ZnO thin films annealed in vacuum, N₂ and O₂. *Phys. B* **388**, 145–152 (2007).
43. Coey, J. M. D. et al. Donor impurity band exchange in dilute ferromagnetic oxides. *Nat. Mater.* **4**, 173–179 (2005).
44. Qi, J. et al. Room-temperature ferromagnetism in Er-substituted ZnO thin films. *Scr. Mater.* **60**, 289–292 (2009).
45. Wang, Q. et al. Vacancy-induced magnetism in ZnO thin films and nanowires. *Phys. Rev. B.* **77**, 205411:1–7 (2008).
46. Inamdar, D. Y. et al. Ferromagnetism in ZnO nanocrystals: doping and surface chemistry. *J. Phys. Chem. C.* **114**, 1451–1459 (2010).
47. Chiou, J. W. et al. Electronic structure of ZnO nanorods studied by angle-dependent x-ray absorption spectroscopy and scanning photoelectron microscopy. *Appl. Phys. Lett.* **84**, 3462–3464 (2004).
48. Selma, E. et al. Study on crystallographic and electronic structure of micrometre-scale ZnO and ZnO:b rods via X-ray absorption fine-structure spectroscopy. *J. Syn. Rad.* **28**, 1–7 (2021).
49. Chiou, J. W. et al. Charge transfer in nanocrystalline-Au / ZnO nanorods investigated by x-ray spectroscopy and scanning photoelectron microscopy. *Appl. Phys. Lett.* **90** (19), 192112:1–4 (2007).
50. Chiou, J. W. et al. Correlation between electronic structures and photocatalytic activities of Nanocrystalline-(Au, Ag, and Pt) particles on the surface of ZnO nanorods. *J. Phys. Chem. C.* **115**, 2650–2655 (2011).
51. Singh, S. B. et al. Observation of the origin of d⁰ magnetism in ZnO nanostructures using X-ray-based microscopic and spectroscopic techniques. *Nanoscale* **6**, 9166–9176 (2014).
52. Dadlani, A. L. et al. Exploring the local electronic structure and geometric arrangement of ALD Zn(O,S) buffer layers using X-ray absorption spectroscopy. *J. Mater. Chem. C.* **3**, 12192–12198 (2015).
53. 53. *Table of Periodic Properties of the Elements.* (Sargent-Welch Scientific, 1980).
54. Chiou, J. W. et al. Electronic structure of the carbon nanotube tips studied by x-ray-absorption spectroscopy and scanning photoelectron microscopy. *Appl. Phys. Lett.* **81**, 4189–4191 (2002).
55. Mott, N. F. The basis of the electron theory of metals, with special reference to the transition metals. *Proc. Phys. Soc. Sec. A* **62**, 416–422 (1949).
56. Chiou, J. et al. Electronic structure of ZnO nanorods studied by angle-dependent x-ray absorption spectroscopy and scanning photoelectron microscopy. *Appl. Phys. Lett.* **84**, 3462–3464 (2004).
57. Singh, J. P. et al. Electronic structure of ZnO nanorods studied by angle-dependent x-ray absorption spectroscopy and scanning photoelectron microscopy. *Sci. Adv. Mater.* **5**, 171–181 (2013).
58. Pérez-Dieste, V. et al. Unoccupied orbitals of 3d transition metals in ZnS. *Phys. Rev. B.* **70**, 085205:1–5 (2013).
59. Ishii, M. et al. Local structure analysis of an optically active center in Er-substituted ZnO thin film. *J. Appl. Phys.* **89**, 3679–3684 (2001).
60. Yamamoto, T. et al. XAFS study of the structure of the silica-supported ytterbium oxide catalyst. *Solid State Commun.* **111**, 137–142 (1999).
61. Ishii, M. et al. The optically active center and its activation process in Er-substituted Si thin film produced by laser ablation. *J. Appl. Phys.* **85**, 4024–4031 (1999).
62. Ishii, M. et al. XANES Analysis of Optical Activation Process of Er in Si:Er₂O₃ Thin Film: Electronic and Structural Modifications around Er. *Jpn. J. Appl. Phys.* **38**, 191–194 (1999).
63. Adler, D. L. et al. Local structure of 1.54- μ m-luminescence Er³⁺ implanted in Si. *Appl. Phys. Lett.* **61**, 2181–2183 (1992).
64. Terrasi, A. et al. Evolution of the local environment around Er upon thermal annealing in Er and Co co-implanted Si. *Appl. Phys. Lett.* **70**, 1712–1714 (1997).
65. Fujikawa, T. et al. Theory of Intrinsic and Extrinsic Plasmon Excitation in Deep Core XPS Spectra. *J. Phys. Soc. Jpn.* **55**, 3244–3257 (1986).
66. Anjana, R. et al. Investigating the evolution of local structure around Er and Yb in ZnO:Er and ZnO:Er, Yb on annealing using X-ray absorption spectroscopy. *J. Appl. Phys.* **123**, 153108:1–11 (2018).
67. Ravel, B. et al. ATHENA, ARTEMIS, HEPHAESTUS: data analysis for X-ray absorption spectroscopy using IFEFFIT. *J. Synchrotron Radiation.* **12**, 537–541 (2005).

Acknowledgements

The author (W.F.P.) would like to thank the National Science and Technology Council (NSTC) of Taiwan for providing financial support for research under the project 112-2112-M-032-009-MY2. SCR acknowledges the “Siksha ‘O’ Anusandhan University” for financial support in publishing this article in this journal. SCR acknowledges the “Siksha ‘O’ Anusandhan University” for financial support in publishing this article in this journal.

Author contributions

DKM designed the project, SD and DKM grown the samples, KHC, WXL, SG performed the XANES/EXAFS detailed experiments, KHC, WXL, SD, DKM, SCR, analysis/interpretations and writing the manuscript. WFP edited and made critical comments on the manuscript and SCR, DKM, SD revised accordingly. All the author(s) discussed the results and commented on the manuscript.

Funding

Open access funding provided by Siksha 'O' Anusandhan (Deemed To Be University), National Science and Technology Council (NSTC) of Taiwan, providing the financial support for research under the project 112-2112-M-032-009-MY2.

Declarations

Competing interests

The authors declare no competing interests.

Additional information

Correspondence and requests for materials should be addressed to S.C.R. or W.F.P.

Reprints and permissions information is available at www.nature.com/reprints.

Publisher's note Springer Nature remains neutral with regard to jurisdictional claims in published maps and institutional affiliations.

Open Access This article is licensed under a Creative Commons Attribution 4.0 International License, which permits use, sharing, adaptation, distribution and reproduction in any medium or format, as long as you give appropriate credit to the original author(s) and the source, provide a link to the Creative Commons licence, and indicate if changes were made. The images or other third party material in this article are included in the article's Creative Commons licence, unless indicated otherwise in a credit line to the material. If material is not included in the article's Creative Commons licence and your intended use is not permitted by statutory regulation or exceeds the permitted use, you will need to obtain permission directly from the copyright holder. To view a copy of this licence, visit <http://creativecommons.org/licenses/by/4.0/>.

© The Author(s) 2025